Reconstruction of fluorescence distribution hidden in biological tissue using mesoscopic epifluorescence tomography

Saskia Björn
Karl-Hans Englmeier
Vasilis Ntziachristos
Ralf Schulz

Reconstruction of fluorescence distribution hidden in biological tissue using mesoscopic epifluorescence tomography

Saskia Björn, Karl-Hans Englmeier, Vasilis Ntziachristos, and Ralf Schulz
Institute for Biological and Medical Imaging (IBMI), Helmholtz Zentrum München, Ingolstädter Landstraße 1,
85764 Neuherberg, Germany

Abstract. Mesoscopic epifluorescence tomography is a novel technique that discovers fluorescence bio-distribution in small animals by tomographic means in reflectance geometry. A collimated laser beam is scanned over the skin surface to excite fluorophores hidden within the tissue while a CCD camera acquires an image of the fluorescence emission for each source position. This configuration is highly efficient in the visible spectrum range where trans-illumination imaging of small animals is not feasible due to the high tissue absorption and scattering in biological organisms. The reconstruction algorithm is similar to the one used in fluorescence molecular tomography. However, diffusion theory cannot be employed since the source-detector separation for most image pixels is comparable to or below the scattering length of the tissue. Instead Monte Carlo simulations are utilized to predict the sensitivity functions. In a phantom study we show the effect of using enhanced source grid arrangements during the data acquisition and the reconstruction process to minimize boundary artefacts. Furthermore, we present *ex vivo* data that show high spatial resolution and quantitative accuracy in heterogeneous tissues using GFP-like fluorescence in B6-albino mice up to a depth of 1100 μm. © *2011 Society of Photo-Optical Instrumentation Engineers (SPIE)*. [DOI: 10.1117/1.3560631]

Keywords: optical devices; fluorescence; scattering; absorption; reflection; tomography.

Paper 10566RR received Oct. 19, 2010; revised manuscript received Feb. 8, 2011; accepted for publication Feb. 10, 2011; published online Apr. 4, 2011.

1 Introduction

Recently we presented an approach to mesoscopic epifluorescence tomography (MEFT), imaging fluorophores emitting in the visible spectrum in reflectance geometry.[1] Simulation studies indicated a high potential to image green fluorescent protein (GFP)-like probes up to a penetration depth of 10 mm. Imaging studies performed on phantoms confirmed the capability to three-dimensionally reconstruct fluorescent objects surrounded by a tissuelike, highly scattering medium at different depths with high resolution. While these results were highly encouraging, the experiments and simulations could not mimic complex *in vivo* imaging situations with heterogeneous tissue structures.

Fluorescence tomography and all derived methods are emerging techniques to estimate fluorescence activity and image probe accumulation in diseases such as Alzheimer's[2] and cancer.[3–6] Imaging systems that are based on transillumination geometries similar to x-ray tomography require probes emitting in the near-infrared due to the deep tissue penetration possible in that wavelength region. However, using transillumination makes it difficult to image larger animals or animals with opaque inclusions such as skin chambers. Existing fluorescence diffuse optical tomography systems that are employed in epifluorescence geometry and can serve this specific application, use a diffusion model for photon propagation.[7] However, the diffusion approximation loses validity close to the surface and in cases of small source-detector separation.[8] Those restrictions are overcome by methods like MEFT and fluorescence laminar optical tomography (FLOT) that are derived from laminar optical tomography (LOT)[9, 10] and employ a reflectance geometry similar to fluorescence microscopy. FLOT utilizes a line scan illumination and has potential to image superficial fluorescence with high sensitivity and penetration depths up to 2 to 3 mm in phantoms and *in vivo*.[11–13]

Frequently, it has been shown that reconstructions performed on uniform grids, chosen inside a region of interest (RoI), leads to artefacts nearby the boundaries. This is caused by the fact that diffuse light probes a large tissue volume; if the probed tissue volume, however, is only partially within the grid for which fluorescence values are reconstructed, measured fluorescence will be fully attributed to the grid, but not to locations outside the grid, increasing fluorescence values close to the grid boundaries. Therefore many groups proposed adaptive grid refinement in the reconstruction process.[14–16] Without using adaptive grid refinements, we have tested different source grid arrangements during the data acquisition and the reconstruction process to minimize boundary artefacts.

To further outline the imaging performance of the previously described MEFT-system, we present herein *ex vivo* imaging studies performed in real, heterogeneous tissue, accurately resolving the presence of a GFP-like fluorescent object at different tissue depths up to 1100 μm, highlighting accurate spatial localization, as well as semiquantitative estimation of fluorescence concentration.

Address all correspondence to Saskia Björn, Helmholtz Zentrum München, Institute for Biological and Medical Imaging, Ingolstädter Landstraße 1, Neuherberg, 85764 Germany. Tel: 49-(0)-89-3187-4452; Fax: 49-(0)-3187-3017; E-mail: saskia.bjoern@helmholtz-muenchen.de

2 Theory

The mesoscopic epifluorescence tomography (MEFT) system, operating in reflectance geometry, utilizes the well-known relation between source-detector distance and overall depth of probed tissue—the larger the distance between illumination spot and detector, the deeper the fluorescent signal can be attributed.[10] Thus, we require different source-detector sensitivity functions for each source-detector pair, describing the contribution of a 3D volume element (voxel) to the current measurement. Required sensitivity functions are calculated using Monte Carlo simulations based on the radiative transfer equation, since the diffusion model is only valid further away from the source.[17,18] Monte Carlo calculations are performed using an adaptation of MCML,[19] assuming homogeneous tissue structure and a semi-infinite volume with one flat surface.

Mathematically, the reconstruction problem is given by $y = Ax$, where $y = \{y_{ij}\}$ is the vector of raw MEFT fluorescence measurements for each source-detector pair ij, and $x = \{x_v\}$ is the 3D volume of fluorescence distribution given for each voxel v. The sensitivity or weight matrix $A = \{A_{ij,v}\}$ is given by source and detector Green's functions as $A_{ij,v} = G^s_{ij,v} \cdot G^d_{ij,v}$, where G^s and G^d denote source and detector sensitivities, respectively (for details see Ref. [1]).

In order to estimate the three-dimensional fluorescence distribution, the sensitivity matrix A is inverted using the iterative LSQR algorithm.[20] The number of iterations is chosen automatically such that the estimated residual $|x'_k - x'_{k+1}| < \tau$, with x' denoting the reconstructed fluorescence bio-distribution, k being the number of iteration and τ an empirically determined threshold.

3 Methods and Materials

3.1 Experimental Setup

The mesoscopic epifluorescence tomography (MEFT) system employs standard optoelectronic components (Fig. 1). The beam of a diode laser-pumped all-solid-state laser with an
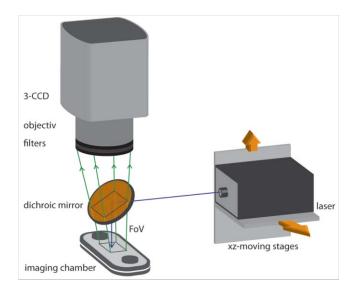

Fig. 1 Schematic setup of the mesoscopic epifluorescence tomography system.

output power of 5 mW at a wavelength of $\lambda = 473$ nm (CNI, Changchun, China) is reflected off a dichroic mirror (Thorlabs, Newton, New Jersey) and scanned over the object's surface using x/z-moving stages (Standa, Vilnius, Lithuania) with a travel range of 25 mm in each direction, to create arbitrary excitation points. Fluorescence emission reflected back into the optical pathway is transmitted through the dichroic mirror due to its longer wavelength, filtered through a long pass color filter (455 nm, Schneider Optik, Bad Kreuznach, Germany) and subsequently collected by a 12-bit 3-CCD camera with a frame rate of 51.5 Hz (Hamamatsu Photonics, Hamamatsu City, Japan) using a 35 mm wide angle lens (Carl Zeiss, Oberkochen, Germany). Acquired images are corrected for dark noise before feeding them into the reconstruction algorithm. To reduce required data storage and computation time, a region of interest in the images is chosen outside of which image data is discarded.

During the *ex vivo* experiments, the imaged specimen is fixed in an imaging chamber, which slightly compresses the animal using an adjustable glass plate, similar to chambers used in other *in vivo* tomographic imaging systems.[21] The chamber guarantees that the animal remains stable and immobilized, without restraining breathing. In addition, using an imaging chamber allows transfer of the animal between imaging systems, e.g., to perform MEFT and x-ray tomography without body movement, making different measurements comparable to each other. Furthermore, the compression creates a defined flat imaging surface on the skin necessary for the currently used reconstruction algorithm.

3.2 Study Preparation

3.2.1 Phantom preparation

A flexible plastic tube ($\varnothing_{inner} = 150~\mu$m, $\varnothing_{outer} = 300~\mu$m, Labmarket GmbH, Mannheim, Germany) was inserted in a tank ($50 \times 100 \times 50$ mm^3) filled with a solution of intralipid, india ink, and water to mimic the strongly absorbing optical properties of tissue in the wavelength region of GFP emission ($\mu_a = 0.1$ mm^{-1}, $\mu_s = 10$ mm^{-1}, anisotropy factor $g = 0.9$). The tube was filled with DiO-dye (3,3′-dioctadecyloxa-carbocyanine perchlorate, MobiTec, Göttingen, Germany) at a concentration of 200 nM mixed with the scattering and absorbing background medium. DiO offers excitation and emission wavelengths ($\lambda_x = 489$ nm, $\lambda_m = 501$ nm) similar to GFP. Successively, the tube was raised in 500 μm steps in the tank to obtain different depths ranging from 200 to 2200 μm.

3.2.2 Animal preparation

Ex vivo studies were performed on two B6-albino mice (Jackson Laboratories, Bar Harbor, Maine) to investigate the potential of MEFT to reconstruct fluorescence distribution in biological tissue. Limitations of optical imaging include the light-absorbing properties of dark hair and skin pigment. The B6-albino mice used in this study maintain the genetic background of the commonly studied B6 mouse without the loss of signal due to dark hair and skin. Four flexible plastic tubes ($\varnothing_{inner} = 150~\mu$m) were filled with DiO-dye at a concentration of 200 nM, as previously described (Sec. 3.2.1). The B6-albino mice were euthanized and their fur was removed. The flexible tubes were fixed on surgical sutures (DS 30/3 metric, Resorba, Nürnberg, Germany)
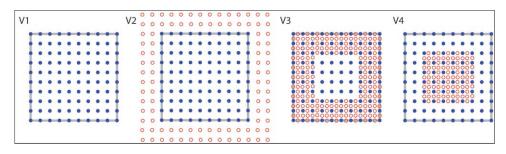
Fig. 2 Source grid arrangements applied in the phantom studies. The defined RoI is marked by a gray square and the blue dots indicate the commonly utilized sources (see V1). V2 shows the measurement series, where additional source positions (red circles) have been placed outside the RoI. V3 and V4 demonstrate the refinement of sources (red circles) that have been embedded in the outer and inner grid. (Color online only.)

and inserted into the muscles of the legs. For detailed *ex vivo* experimental results and analysis, one single, exemplary data set (mouse 1, right leg) is presented to estimate how well arbitrary objects at different depths can be reconstructed by the proposed method. Analogous values of the four different series of measurements are calculated and presented for comparison.

3.3 Experimental Setting

3.3.1 Phantom study

The region of interest was defined as a square with side lengths of 5000 μm (see Fig. 2). A grid of 10×10 source positions with a spacing of 500 μm [indicated by blue dots in Fig. 2(V1)] was placed on the RoI [indicated by the gray square in Fig. 2(V1)]. The measured data volume thus consisted of 100 images at the intrinsic CCD resolution of 1024×1344 pixels. For the second series of measurements, we added further sources outside of the RoI [see Fig. 2(V2)] and accordingly acquired 196 images. Figure 2(V3) indicates the third setting, where the outer grid was refined by positioning additional sources with a spacing of 250 μm (red circles) and thus yielded a data volume of 296 images. Figure 2(V4) shows the complementary situation, where the inner source grid was refined. This led to a data set of 185 images. To reduce the amount of data fed into the reconstruction process, images were reduced by a factor of ten using bicubic interpolation, and a region of interest was chosen inside the images. The resulting image pixels were used as detector positions in the reconstruction algorithm. Numbers of iterations between 50 and 90 were automatically chosen as described above, refer to Sec. 2. Depending on the detected signals, exposure times were set between 4 ms for a tube depth of 200 μm and 40 ms for a tube depth of 2200 μm. However, the exposure time was held constant for all measurements at one tube depth. To acquire purely planar epifluorescence images as control data, an expanded laser beam was used for image acquisition. Beam widening was achieved using a light diffuser (Luminit, Torrance, California) and led to a spot full width at half maximum of 24.7 mm.

3.3.2 Ex vivo study

The exposure time t for an *ex vivo* measurement at one source position was automatically determined to make optimal use of the CCD's dynamic range. Exposure times were set between 5 ms and 3500 ms, depending on the 95th percentile of signal intensities in the green channel of the 3-CCD camera, as

described by $P_{95}(I_{G,\text{control}} - I_{G,\text{background}})/t_{\text{control}} \cdot I_{G,\text{desired}} = t$. For each laser position, a first control image $I_{G,\text{control}}$ with an exposure time of $t_{\text{control}} = 10$ ms, was acquired to estimate the maximum signal intensity. $I_{G,\text{background}}$ denotes the dark noise used to correct the green channel of the colour image, for which the 95th percentile P_{95} was calculated. The desired intensity $I_{G,\text{desired}}$ was defined as the maximum intensity of 3900 photon counts. This desired maximum was chosen well below the saturation limit of 4096 photon counts (based on the 12-bit CCD employed).

A grid of 11×11 source positions separated by 500 μm in each direction was used in the imaging experiments. The measured data volume thus consisted of 121 images at 1024×1344 pixel resolution. As described in Sec. 3.3.1, we reduced the data fed into the reconstruction process and chose a RoI within the source grid arrangement similar to Fig. 2(V2), where the boundaries were excluded. Purely planar epifluorescence images were acquired as control data and the numbers of iterations (between 50 and 100) were automatically chosen as described in Sec. 2.

The contrast to noise ratio $C = |I_1 - I_2| \cdot \sigma^{-1}$ was calculated to evaluate signal quality, with I_1 and I_2 being the 95th percentile and 5th percentile of the maximum intensity, respectively, and σ denoting the standard deviation of the noise in the dark image.

Additionally, the leakage of excitation light was measured by exciting the shaved skin of the animal prior to inserting any fluorescent inclusion. The 95th percentile of the maximum intensity in the accordingly detected raw image was measured for exposure times ranging from 1 ms up to 3500 ms.

3.4 Validation of the Ex Vivo Results

To validate the reconstructed depth of the tube, we sectioned the imaged tissue and subsequently performed white light and fluorescence imaging using a modified cryoslicer system.[22] For each measurement, the respective field of view (FOV) of the camera was marked on the skin of each mouse. Directly after the MEFT imaging session, the mice were frozen within the imaging chamber at $-20°$C to ensure that the geometry would not change between MEFT imaging and cryoslicing. Subsequently, the mice were removed from the chamber, and the tissue regions within the FOV of the measurements were embedded in optimal cutting temperature compound (OCT) and refrozen to $-80°$C. Afterwards, the tissue samples were cut in slices at a thickness of 250 μm, during which a white light image as well as a filtered fluorescence image was acquired for each slice. From the images, the depth and position of the fluorescent tube could be
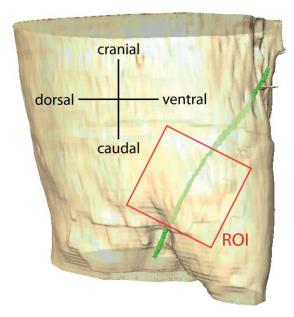
Fig. 3 Merged surefaceplots of the abdomen and inserted fluorescent tube (green) shown in the perspective of the camera (mouse 1, right leg). Additionally the region of interest and the anatomical orientations are indicated. (Color online only.)

Fig. 4 The results of the phantom study are exposed for each tube depth (rows) and source grid arrangement (columns) in this table. In the first row the epifluorescence images and their line profiles, which were detected orthogonally to the middle of the fluorescent tube, are shown. Slices of the reconstructed tube, following the center of the reconstructed fluorescence distribution, are presented in the rows V1-V4 utilizing the source grid arrangement V1-V4.

accurately extracted as shown in Fig. 6(d). Furthermore, we used the cryosection images to create a surface plot of the abdomen of mouse 1 and the fluorescent tube that was inserted in its right leg. To get an impression of the perspective of the camera, the merged surface plots are shown in Fig. 3. Additionally the RoI and the anatomical orientations are indicated.

4 Results

4.1 *Phantom Studies*

The reconstruction results for the phantom study are shown in Fig. 4 for each tube depth (rows in the figure) and source grid arrangement (columns in the figure). In the first row, the epifluorescence images and their line profiles, which were detected orthogonal to the middle of the fluorescent tube, are shown. The full width at half maximum (FWHM) in the middle of the tube at a depth of 200 μm was detected as $\text{FWHM}_{200\,\mu\text{m}} = 246\ \mu$m and increased up to a $\text{FWHM}_{2200\,\mu\text{m}} = 780\ \mu$m measured for a depth of 2200 μm. Slices of the reconstructed fluorescence distribution, following the center of the tube, are presented in the rows of the figure. Data acquisition and reconstruction performed with the source grid arrangement that is shown in Fig. 2(V1) lead to significantly improved reconstructions of shape and dimension of the tube (V1, $\text{FWHM}_{200\,\mu\text{m}} = 147\ \mu$m and $\text{FWHM}_{2200\,\mu\text{m}} = 290\ \mu$m) as compared to the raw epifluorescence images. The results [Fig. 2(V2), $\text{FWHM}_{200\,\mu\text{m}} = 154\ \mu$m and $\text{FWHM}_{2200\,\mu\text{m}} = 284\ \mu$m] of the enlarged source grid arrangement [Fig. 2(V2)] are comparable to the previous row Fig. 2(V1), but the boundary artifacts have been removed. However, in the case of imaging a limited area, e.g., the leg, some source-detector pairs of the enlarged source grid arrangement [Fig. 2(V2)] might be positioned outside of the tissue, which would lead to additional artefacts. One possible solution to overcome this limitation would be to refine the peripheral
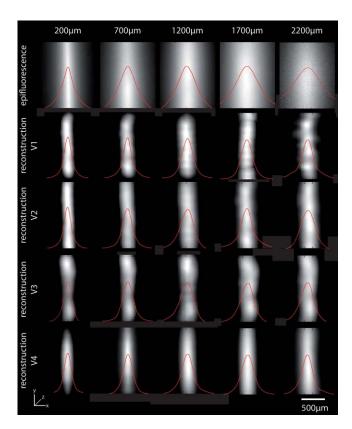
grid by placing additional sources within the region of interest instead of outside the RoI, as shown in [Fig. 2(V3)]. However, the accuracy of reconstructions in fact deteriorated as boundary values of the RoI were imprecisely reconstructed ($\text{FWHM}_{200\,\mu\text{m}} = 150\ \mu$m and $\text{FWHM}_{2200\,\mu\text{m}} = 209\ \mu$m). This behaviour can be explained easily as for sources and detectors located on the periphery, measurements are always fully attributed to the region of interest, but not to effects from outside this area. Therefore, the increased amount of measurements that detect signals coming from outside the RoI led to an increase in boundary artifacts. That finding led to the fourth arrangement [Fig. 2(V4)], where the inner source grid has been refined. Due to the additional sources in the inner volume, this area received a stronger weight during the reconstruction process. When reconstructing the tube at a depth of 200 μm, this source grid refinement has a negative impact, since the boundary areas are imprecisely reconstructed. However, the deeper the tube is covered in the surrounding material, the higher is the benefit of the source grid arrangement V4 [see Fig. 2(V4)] on the accuracy of the reconstructed shape and fluorescence distribution ($\text{FWHM}_{200\,\mu\text{m}} = 149\ \mu$m and $\text{FWHM}_{2200\,\mu\text{m}} = 267\ \mu$m).

Due to the improved source grid arrangements, the data acquisition and reconstruction process are more time consuming. Data acquisition took t = 4 to 5 sec per source position, which led to a total acquisition time for one complete data set of t_{V1}

= 9 min (V1) up to t_{V3} = 24 min (V3). The reconstruction time for the enlarged volume [Fig. 2(V2)] or additional measurements [Figs. 2(V3) and 2(V4)] was measured as t_{V1} = 9 min (V1), t_{V2} = 31 min [Fig. 2(V2)], t_{V3} = 26 min [Fig. 2(V3)] and t_{V4} = 17 min [Fig. 2(V4)] per iteration.

To validate the phantom study using different source grid arrangements, a more quantitative analysis is presented in Fig. 5. The fluorescence distributions at a depth of 1200 μm along the tube are shown in Fig. 5(a). The solid line indicates the fluorescence signal at the center of the tube in the epifluorescence measurement. Accordingly, the reconstructed fluorescence concentrations using the source grid arrangement V1 (dashed curve), V2 (dotted line), V3 (line with diamonds), and V4 (line with circles) are presented. It can be seen that the variation of the detected fluorescence distributions measured in the epifluorescence image is negligible. This is due to the constant tube depth and homogeneous optical properties of the surrounding material. The source grid arrangement V1 leads to a steep drop of reconstructed fluorescence intensity at the grid boundaries to less than 60% of the maximum intensity. Utilizing the source grid arrangement V2 provides the best result, as the reconstructed fluorescence distribution is continuously more than 94% of the maximum. V3 yields a drop at the center of the tube to less than 80% of the maximum fluorescence distribution. This effect is due to the refined and thus higher weighted boundaries. The fluorescence distribution given by the source grid arrangement V4, drops to 90% at the boundaries. This effect is due to the refined and accordingly higher weighted inner volume. However, the benefit of the source grid arrangement V4 increases for deeper tube locations, as shown in Fig. 4. In Fig. 5(b), the actual tube diameter (line with dot markers) and the reconstructed values are plotted. The FWHM of the observed epifluorescence signal versus the tube depth is presented as a solid line. To obtain values of the reconstructed diameter using the source grid arrangements V1 (dashed line), V2 (dotted line), V3 (line with diamonds), and V4 (line with circles), the FWHM of the reconstructed tube was determined in the *x*- and *z*-direction for each slice along the tube (*y*-direction). The voxel values were averaged to obtain the signal values for each source depth. The FWHM in the planar image is, on average, more than three times larger than the actual tube diameter. However, the FWHMs of the reconstructions correspond well with the actual values, where the source grid arrangement V1 leads to the largest error at a depth of 2200 μm. In Fig. 5(c), the actual depth of the tube (solid line with dot markers) is plotted versus the average depth of the reconstructed fluorescence distribution. The reconstructed tube depths using the source grid arrangement V1 (dashed line), V2 (dotted line), V3 (line with diamonds), and V4 (line with circles) lead to similar results, where the localization error rises with increasing depth. The maximum error of 9% is obtained at a depth of 2200 μm for the reconstruction using the source grid arrangement V1.

4.2 *Ex Vivo Studies*

The results of the *ex vivo* measurements of mouse 1 (right leg) are presented in Fig. 6. The epifluorescence measurement is shown in Fig. 6(a). The intensity of the fluorescent signal strongly decays along the *y*-direction, corresponding to the increasing
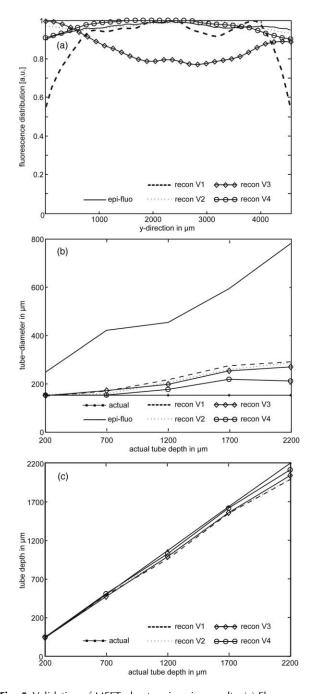

Fig. 5 Validation of MEFT phantom imaging results. (a) Fluorescence distribution in a depth of 1200 μm along the tube. The solid line depicts the relative fluorescence intensity in the epifluorescence imaging along the center of the tube. The reconstructed fluorescence concentration using the source grid arrangement V1 (dashed line), V2 (dotted line), V3 (line with diamonds), and V4 (line with circles) are presented. All curves were normalized to their respective maximum value. (b) Plot of the FWHM of the reconstructed tube diameter for different tube depths. The horizontal line with dot markers depicts the actual tube diameter of 150 μm. The solid line indicates the tube diameter in the epifluorescence image. To obtain the values of the reconstructed diameter using the source grid arrangement V1 (dashed line), V2 (dotted line), V3 (line with diamonds), and V4 (line with circles) the FWHM of the reconstructed tube was determined in the *x*- and *z*-direction for each slice along the tube (*y*-direction). The voxel values were averaged to obtain the signal values for each source depth. (c) Reconstructed depth in comparison to actual depth (solid line with dot markers). The dashed line indicates the source grid arrangement V1, the dotted line, V2, the line with diamonds, V3, and the line with circles, V4.
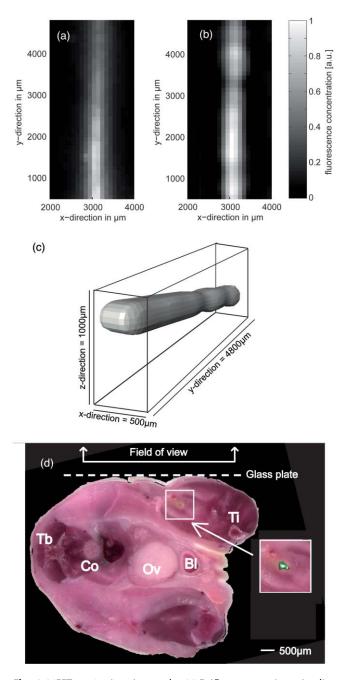
Fig. 6 MEFT *ex vivo* imaging results. (a) Epifluorescence intensity distribution. (b) Angular slice of reconstructed fluorescence distribution along the depth of the tube center. (c) Three-dimensional rendering of the reconstructed fluorescent tube. The box depicts the dimension and localization of the reconstructed tube. (d) White light cryoslice image where the tube reached a depth of 640 μm. The rectangular inset shows a magnification of the area of the fluorescent tube, where the green false color shows an overlay of the fluorescence distribution detected in the cryoslicer. Additionally the tail bone (Tb), the tibia (Ti), the colon (Co), the ovary (Ov) and the bladder (Bl) are indicated.

depth at which the fluorescent tube was located. In comparison, Fig. 6(b) depicts an angular slice through the reconstructed volume, following the center of the reconstructed fluorescence distribution. Although some slight variation in intensity can be observed, it occurs independently of depth and, overall, the signals within the reconstructed tube are more homogeneous than

in Fig. 6(a) and the tube has a focused appearance. To visualize the location of the fluorescent tube in the reconstructed 3D volume stack, a surface plot of the reconstructed fluorescence distribution is presented in Fig. 6(c). The colorbar in the grayscale images was normalized to the maximum intensity in the images.

As an example, the image of the cryoslicer section that was taken at 2500 μm in the *y*-direction [Fig. 6(b)] is shown in Fig. 6(d). The field of view (FOV) and the position of the glass plate are indicated. It can be observed that the skin surface, although compressed by the glass plate, was not perfectly flat. Skin folds within the field of view, however, were less than 250 μm in depth. The rectangle marks the area where the fluorescent tube was located. The corresponding region is enlarged, featuring (in green) the overlay of the fluorescence as detected in the cryoslicer. Additionally, the tibia (Ti), the tail bone (Tb), the colon (Co), the ovary (Ov) and the bladder (Bl) are indicated to get a sense of the tube location inside the mouse.

To validate the reconstruction of mouse 1 (right leg) obtained by MEFT imaging in a more quantitative manner, different analyses are presented in Fig. 7. The fluorescence signal or estimated concentration along the tube (*y*-direction) is shown in Fig. 7(a). The solid line shows the fluorescence signal from the center of the tube in the epifluorescence measurement. The dashed curve depicts the MEFT-reconstructed fluorescence concentrations along the tube. To obtain these values, at first the FWHM of the reconstructed tube was determined in the *x*- and *z*-directions for each slice along the *y*-axis. Within this area, voxel values were averaged to obtain the signal values in the figure. Again, the intensities in the epifluorescence image are strongly correlated with inclusion depth, while the reconstructed concentrations relate well to the true situation. Figure 7(b) depicts the FWHM of the observed signals for the planar epifluorescence image (solid line) as well as for the *x*- (dotted line) and *z*-axis (dashed line) in the 3D volume stack in comparison to the actual diameter of the tube (solid line with dots). While the FWHM in the planar image is, on average, more than three times larger even though the tube is located less than 1 mm underneath the skin, the FWHM in the reconstruction corresponds well with the true values. Along the x-axis, the average diameter is reconstructed as 231 μm, while the reconstruction along the *z*-direction has a greater accuracy (170 μm). In Fig. 7(c), the depth of the tube as obtained by image analysis on the cryoslicer images (solid line with dots) is plotted versus the average depth in the reconstructed volume (dashed line). With increasing depth, the localization error increases accordingly, but remains well below 10% up to a depth of 1000 μm.

The three additional measurements, where the extra fluorescent tubes have been analyzed, show similar results. Mouse 1 (left leg) showed a strong correspondence between the tube depth obtained in the cryoslicer images and the reconstructed depth (error < 5%). However, in this case the maximum tube depth in the RoI was 850 μm. Mouse 2 (right leg) presented a nearly constant tube depth in the RoI of 500 μm to 550 μm in the cryoslicer images as well as in the reconstructions (error < 5%). For the RoI of Mouse 2 (left leg), the tube depth obtained in the cryoslicer images was measured between 300 μm and 900 μm. Again, we found the localization error increases with depth, but remains between 2% and 10%. Additionally, we calculated the contrast to noise ratio CNR
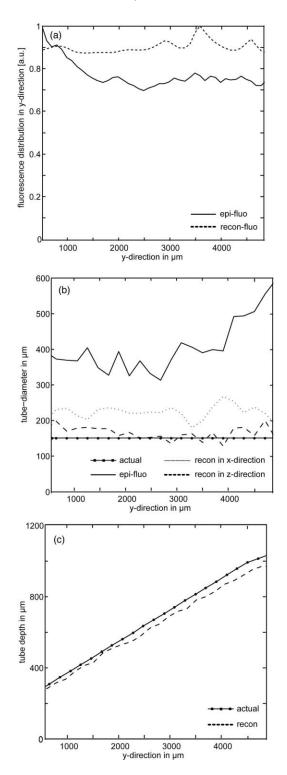
Fig. 7 Validation of MEFT *ex vivo* imaging results. (a) Fluorescence distribution along the tube length (*y*-direction). The solid line depicts the relative fluorescence intensity in the epifluorescence imaging along the center of the tube. The dashed curve shows the corresponding reconstructed fluorescence concentrations. Both curves were normalized to their respective maximum values. (b) Plot of the reconstructed tube diameter (FWHM) for different depths of the tube. The horizontal line with dot markers depicts the actual tube diameter of 150 μm. The solid line indicates the tube diameter in the epifluorescence image. The dashed curve shows the reconstructed diameter in *z*-direction and the dotted in *x*-direction. (c) Reconstructed depth in comparison to actual depth. The solid line with dots indicates the actual and the dashed curve the reconstructed depths.

= 12401, which is an adequate value for reconstruction purposes.[1] The leakage of excitation light alternated between 150 and 200 photon counts. These values are negligible compared to the background levels that are subtracted.

5 Discussion and Outlook

We have shown the strong potential of the mesoscopic epifluorescence tomography system to reconstruct fluorescence distributions in the visible wavelength range with a high depth sensitivity and accuracy up to a depth of 1000 μm in heterogeneous tissue.

Fluorescence confocal microscopy (FCM) is a well known optical imaging technique used to increase the optical resolution and the contrast of microscopes by using point illumination and a spatial pinhole to eliminate out-of-focus light in specimens that are thicker than the focal plane.[23,24] Dependent on the wavelength used, FCM excited by a 488 nm beam, offers a high resolution in the *x*- and *y*-direction of around 200 nm, but a penetration depth that is limited to a few hundred micrometers.[25] As much of the light from sample fluorescence is blocked at the pinhole, the increased resolution is at the cost of decreased signal intensity, often leading to increased exposure times. The presented phantom and *ex vivo* studies have shown that MEFT imaging offers penetration depths deeper than 2000 μm and high fluorescence intensities using exposure times of less than 50 ms.

Yuan et al. have shown co-registered results of OCT and line-scan FLOT.[12] A capillary tube (ø$_{inner}$ = 100 μm) filled with 10 μM fluorescent dye, Cy5.5, has shown good results of its reconstructed depths of 600 and 900 μm. However, the contour and diameter of the tube and the fluorescence concentration were barely observable in the FLOT images. MEFT reconstructions offer accurate information about (at least relative) fluorescence intensity, inclusion size, and localization, although the considered tissue depths are well below what is feasible using near-infrared tomography. Resulting images are significantly more accurate in terms of spatial resolution and fluorescence intensity than what is observed in planar fluorescence images, which resemble the de facto gold standard in biological imaging. Spatial resolution is furthermore, far better than what would be achievable using whole-body fluorescence tomography, which would remain challenging due to the wavelength used here. Zacharakis et al. have shown the feasibility of whole-body tomography in the visible wavelength range. However, in the case of *in vivo* imaging, the utilized laser power of 40 mW and fluorescein isothiocyanate concentration of 500 to 4000 nM were comparatively high.[26]

Different source grid arrangements have been analyzed in a detailed phantom study. We found that the accuracy of MEFT and possibly other epifluorescence imaging modalities can be significantly improved when imaging and reconstructing an enlarged volume and afterwards excluding the periphery.

In order to avoid further artefacts, in the case of imaging a limited area, refining the inner source grid has a significant benefit when imaging objects deeper seated than 1200 μm in the tissue. The additional expenditure of time using the V2 (Fig. 2) source grid arrangement in the data acquisition and reconstruction process should be considered, when choosing the most favorable imaging and reconstruction protocol (Fig. 2).

To summarize, MEFT is an interesting and accurate alternative to whole-body tomography when superficial lesions need to be observed with high resolution and accuracy, or where other factors prevent transillumination of a whole animal, such as short wavelength probes, opaque imaging obstacles such as skin chambers, and the like.

One possible limitation of the proposed technique might be the use of compression to gain a flat imaging surface. In principle it is possible to use curved surfaces for the Monte Carlo simulations to obtain a more accurate forward model. Considering the size of the field of view being only a few millimeters in the current system, there might not be a need for a more accurate shape, however, even for strongly curved body parts such as the skull, it will be possible to find an area of sufficient flatness for imaging. In the presence of skin chambers, of course, this is no longer a concern. Furthermore we could demonstrate accurate reconstruction results even in the presence of skin folds, i.e., when the surface was not perfectly flat.

The system is intended for three-dimensional reconstruction of the fluorescence bio-distribution, however, only a single concentration was used, and thus reconstructed concentrations were solely validated for homogeneity. To reach absolute, inter-subject quantifiability, a next step will be to develop normalization methods utilizing the color information of the 3-CCD camera. Furthermore, we will focus on *in vivo* measurements and include combined green and red fluorescent protein (RFP) measurements using excitation light at 473 and 532 nm along with the related filter sets. Mesoscopic epifluorescence tomography has a strong potential to be included into existing systems, e.g., confocal microscopes, or endoscopic setups as used in the clinics. Beside the enhancement of the MEFT system, future work will concentrate on feasible clinical applications and their realization.

References

1. S. Björn, V. Ntziachristos, and R. Schulz, "Mesoscopic Epifluorescence Tomography: Reconstruction of superficial and deep fluorescence in highly-scattering media," *Opt. Exp.* **18**(8), 8422–8429 (2010).
2. D. Hyde, R. de Kleine, S. A. MacLaurin, E. Miller, D. H. Brooks, T. Krucker, and V. Ntziachristos, "Hybrid FMT-CT imaging of amyloid-[beta] plaques in a murine Alzheimer's disease model," *Neuroimage* **44**(4), 1304–1311 (2009).
3. A. Koenig, L. Herve, V. Josserand, M. Berger, J. Boutet, A. Da Silva, J. M. Dinten, P. Peltie, J. L. Coll, and P. Rizo, "*In vivo* mice lung tumor follow-up with fluorescence diffuse optical tomography," *J. Biomed. Opt.* **13**(1), 011008 (2008).
4. N. Deliolanis, T. Lasser, D. Hyde, A. Soubret, J. Ripoll, and V. Ntziachristos, "Free-space fluorescence molecular tomography utilizing 360 degrees geometry projections," *Opt. Lett.* **32**(4), 382–384 (2007).
5. A. Da Silva, M. Leabad, C. Driol, T. Bordy, M. Debourdeau, J. M. Dinten, P. Peltie, and P. Rizo, "Optical calibration protocol for an x-ray and optical multimodality tomography system dedicated to small-animal examination," *App. Opt.* **48**(10), D151–D162 (2009).
6. D. Kepshire, N. Mincu, M. Hutchins, J. Gruber, H. Dehghani, J. Hypnarowski, F. Leblond, M. Khayat, and B. W. Pogue, "A microcomputed tomography guided fluorescence tomography system for small animal molecular imaging," *Rev. Sci. Instrum.* **80**(4), 043701 (2009).
7. D. Kepshire, S. C. Davis, H. Dehghani, K. D. Paulsen, and B. W. Pogue, "Fluorescence tomography characterization for sub-surface imaging with protoporphyrin IX," *Opt. Exp.* **16**(12), 8581–8593 (2008).
8. T. J. Farrell, M. S. Patterson, and B. Wilson, "A diffusion theory model of spatially resolved, steady-state diffuse reflectance for the noninvasive determination of tissue optical properties in vivo," *Med. Phys.* **19**(4), 879–888 (1992).
9. E. M. C. Hillman, D. A. Boas, A. M. Dale, and A. K. Dunn, "Laminar optical tomography: Demonstration of millimeter-scale depth-resolved imaging in turbid media," *Opt. Lett.* **29**(14), 1650–1652 (2004).
10. E. M. C. Hillman and S. A. Burgess, "Sub-millimeter resolution 3D optical imaging of living tissue using laminar optical tomography," *Laser Phot. Rev.* **3**(1–2), 159–179 (2009).
11. B. Yuan, S. A. Burgess, A. Iranmahboob, M. B. Bouchard, N. Lehrer, C. Bordier, and E. M. C. Hillman, "A system for high-resolution depth-resolved optical imaging of fluorescence and absorption contrast," *Rev. Sci. Instrum.* **80**(4), 043706 (2009).
12. S. A. Yuan, Q. Li, J. Jiang, A. Cable, and Y. Chen, "Three-dimensional coregistered optical coherence tomography and line-scanning fluorescence laminar optical tomography," *Opt. Lett.* **34**(11), 1615–1617 (2009).
13. Y. Chen, S. Yuan, J. Wierwille, C.-W. Chen, T. Blackwell, P. Winnard, V. Raman, and K. Glunde, "Integrated Optical Coherence Tomography (OCT) and Fluorescence Laminar Optical Tomography (FLOT) for Depth-Resolved Subsurface Cancer Imaging in Biomedical Optics (BIOMED)," *Opt. Soc. Am.* (2010).
14. J. Condell, B. Scotney, and P. Morrow, "Adaptive grid refinement procedures for efficient optical flow computation," *Intern. J. Comp. Vision* **61**(1), 31–54 (2005).
15. A. Joshi, W. Bangerth, and E. Sevick-Muraca, "Adaptive finite element based tomography for fluorescence optical imaging in tissue," *Opt. Exp.* **12**(22), 5402–5417 (2004).
16. M. Guven, B. Yazici, K. Kwon, E. Giladi, and X. Intes, "Effect of discretization error and adaptive mesh generation in diffuse optical absorption imaging: II.," *Inverse Problems* **23**, 1135 (2007).
17. A. Dunn and D. Boas, "Transport-based image reconstruction in turbid media with small source-detector separations," *Opt. Lett.* **25**(24), 1777–1779 (2000).
18. S. L. Jacques and B. W. Pogue, "Tutorial on diffuse light transport," *J. Biomed. Opt.* **13**(4), 041302 (2008).
19. L. Wang, S. L. Jacques, and L. Zheng, "MCML–Monte Carlo modeling of light transport in multi-layered tissues," *Comput. Meth. Prog. Biomed.* **47**(2), 131–46 (1995).
20. C. C. Paige and M. A. Saunders, "LSQR: An algorithm for sparse linear equations and sparse least squares," *ACM Trans. Math. Software (TOMS)* **8**(1), 43–71 (1982).
21. E. E. Graves, J. Ripoll, R. Weissleder, and V. Ntziachristos, "A sub-millimeter resolution fluorescence molecular imaging system for small animal imaging," *Med. Phys.* **30**(5), 901–911 (2003).
22. A. Sarantopoulos, G. Themelis, and V. Ntziachristos, "Imaging the Bio-Distribution of Fluorescent Probes Using Multispectral Epi-Illumination Cryoslicing Imaging," *Mol. Imag. Biol.* 1–12 (2010).
23. J. B. Pawley and B. R. Masters, "Handbook of biological confocal microscopy," *J. Biomed. Opt.* **13**, 029902 (2008).
24. Y. Li, S. Gonzalez, T. H. Terwey, J. Wolchok, Y. Li, I. Aranda, R. Toledo-Crow, and A. C. Halpern, "Dual mode reflectance and fluorescence confocal laser scanning microscopy for in vivo imaging melanoma progression in murine skin," *J. Invest. Derm.* **125**(4), 798–804 (2005).
25. E. Botzung-Appert, V. Monnier, T. Ha Duong, R. Pansu, and A. Ibanez, "Polyaromatic luminescent nanocrystals for chemical and biological sensors," *Chem. Mater.* **16**(9), 1609–1611 (2004).
26. G. Zacharakis, J. Ripoll, R. Weissleder, and V. Ntziachristos, "Fluorescent protein tomography scanner for small animal imaging," *Med. Imag. IEEE Trans.* **24**(7), 878–885 (2005).